https://doi.org/10.38124/ijisrt/25nov252

# Modeling the Thermomechanical Behavior of a Metallic Bellows: Case of Stainless Steel 1.4571 and Inconel 718

Alhadji Laouane Kadi Taousset<sup>1,2</sup>; Jacob Houyouk<sup>1</sup>; Guy Edgar Ntamack<sup>1</sup>; Alexis Kuitche<sup>2</sup>

<sup>1</sup>Mechanics, Materials and Acoustics, P.O. Box 454, Department of Physics, Faculty of Science, University of Ngaoundéré, Cameroon

<sup>2</sup>National School of Agro-Industrial Sciences, P.O. Box 454, Department of Mechanical Engineering, University of Ngaoundéré, Cameroon

Publication Date: 2025/11/12

Abstract: This study aims to evaluate the thermomechanical stresses to which bellows may be subjected in order to make a judicious choice of the appropriate material for its manufacture and improve its lifespan. To do this, thermomechanical stresses are determined as a function of mechanical and thermal loads. By varying certain geometric and technical parameters, we evaluated the stresses and displacements. We used the State-Space method to determine the state equation and the state matrix in order to numerically determine the intrinsic and extrinsic behaviors of the materials. The different numerical simulations using the finite element method on Abaqus/CAE allowed us to determine the maximum thermomechanical stress for each type of material. The weakening criterion between the mechanical and thermal stresses and the lifespans under thermomechanical stress for the cases of Stainless Steel 1.4571 and Inconel 718 materials are identified and make it possible to choose the material for the manufacture of the metal bellows.

Keywords: Metallic Bellows, Thermomechanical Stress, Lifespan, Abaqus.

**How to Cite :** Alhadji Laouane Kadi Taousset; Jacob Houyouk; Guy Edgar Ntamack; Alexis Kuitche (2025). Modeling the Thermomechanical Behavior of a Metallic Bellows: Case of Stainless Steel 1.4571 and Inconel 718. *International Journal of Innovative Science and Research Technology*, 10(11), 234-247. https://doi.org/10.38124/ijisrt/25nov252

## I. INTRODUCTION

Bellows-sealed globe valves are commonly used in industrial thermal hydraulic systems for applications involving superheated steam and thermal oil. The bellows' material must withstand both corrosion and high temperatures. Stresses on the bellows are influenced by its geometry and applied loads, such as pressure and torsional force. By comparing these calculated stresses to the material's allowable limits, safety factors can be determined for stainless steel 1.4571 and Inconel 718.

Previous research, such as Anatoly's work [1], has explored the superalloy Inconel 718, focusing on selective laser melting and its effects on microstructure and mechanical properties. Other studies have investigated the use of laser fusion technology on Inconel 939, linking changes in microstructure and residual stresses to process parameters [3-6]. Experimental data on austenitic stainless steel 1.4571 has also been collected at varying temperatures to determine key mechanical properties like tensile strength and creep behavior

[7-12]. While these studies have been valuable, they often relied on finite element methods and experiments without focusing on a comprehensive lifecycle analysis.

More recent work, using Directed Energy Deposition (DED) processes, has examined how substrate properties like hardness and slope affect the thermomechanical characteristics of deposited Inconel 718, aiming to improve component reliability [13-20].

This paper's contribution is to model the thermomechanical behavior of bellows made from Inconel 718 and stainless steel 1.4571. The goal is to identify a damage criterion between mechanical and thermal stress and determine the parameters necessary to optimize the valve's lifespan. The study is structured to present the state-space method, followed by numerical results from Abaqus and Matlab, concluding with a synthesis of the findings.

https://doi.org/10.38124/ijisrt/25nov252

#### II. MATERIALS AND METHODS

#### ➤ Materials

For this study, Abaqus/CAE and Matlab were used to perform various simulations. The primary components of our research are metallic bellows, which are thin-walled cylindrical parts with a corrugated surface. These bellows are manufactured by hydraulically forming thin-walled tubes.

Bellows can be single-walled, which have low stiffness and are typically used in vacuum technology, or multi-walled. Multi-walled bellows offer both high pressure resistance and great flexibility, making them ideal for high-stress applications like valve stem seals, which can operate at pressures exceeding 400 bar. The design, including the number of walls, is determined by the specific application's requirements [21].

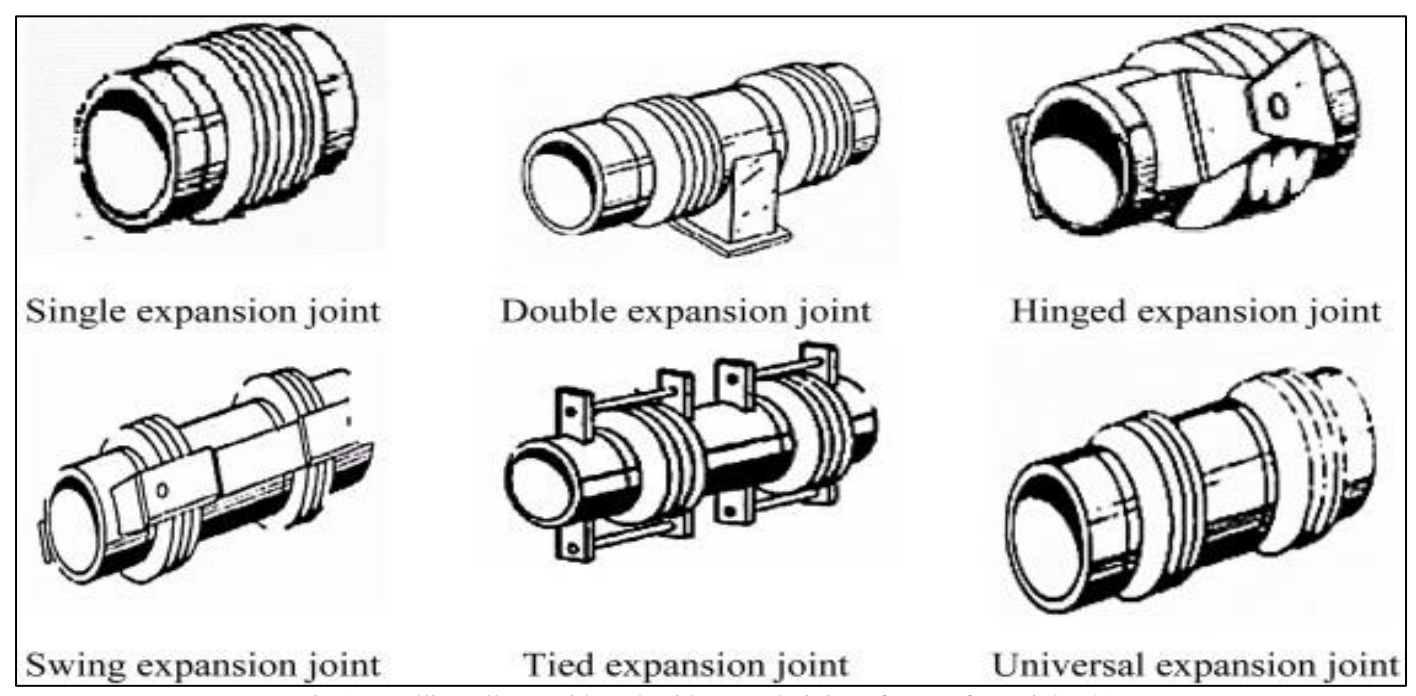


Fig 1 Metallic Bellows with and Without end Fittings from Left to Right [21]

## > Mathematical Formulation

# • Geometry and Problem Formulation

The metallic bellows is represented in its structural form in figure 2 below, which has ten (10) convolutions with a three (03) mm thread separating each convolution, both internal and external.

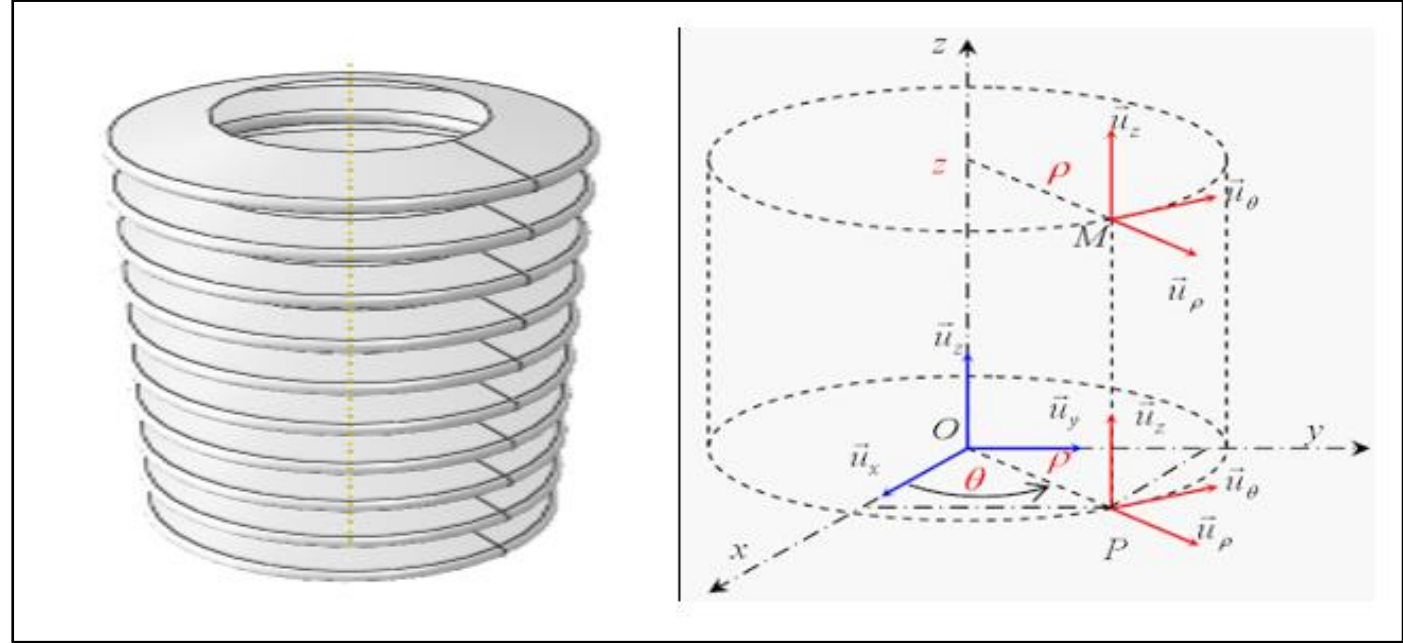


Fig 2 Geometry of the Problem

https://doi.org/10.38124/ijisrt/25nov252

The thermomechanical behavior of the system is governed by the law given by equation (1):

$$\sigma_{ij} = C_{ijkl} \varepsilon_{kl} - \beta_{ij} T \tag{1}$$

It represents the equation of motion, which will be solved using the state-space method. It is particularly important to understand the behavior of structures to evaluate their service life. Throughout their lifecycle, these structures are required to withstand various stresses and highly corrosive environments [22]. Therefore, modeling requires an appropriate approach. For this study, we use the state-space method, a mathematical technique for solving systems of dynamic equations. It transforms a system of partial differential equations into a first-order matrix system. This method is used in virtually all research fields involving dynamic systems, such as materials mechanics, electronics,

and control engineering [23]. Dynamic models with linear factors, or state-space models, constitute an empirical class [24].

In the cylindrical coordinate system, the linearized constitutive equations for an orthotropic cylindrical structure can be presented using the three-dimensional generalized Hooke's law as follows [25]:

#### • State-Space Method

Physical systems are governed by complex equations that can be difficult to solve. Numerical methods are often used to simplify these problems. In our study, we employed the state-space method.

For an isotropic material, the equation of motion given in relation (1) is written in matrix form as follows:

$$\begin{bmatrix} \sigma_{rr} \\ \sigma_{\varphi\varphi} \\ \sigma_{zz} \\ \tau_{\varphiz} \\ \tau_{r\varphi} \end{bmatrix} = \begin{bmatrix} Q_{11} & Q_{12} & Q_{13} & 0 & 0 & 0 \\ Q_{21} & Q_{22} & Q_{23} & 0 & 0 & 0 \\ Q_{13} & Q_{23} & Q_{33} & 0 & 0 & 0 \\ 0 & 0 & 0 & Q_{44} & 0 & 0 \\ 0 & 0 & 0 & 0 & Q_{55} & 0 \\ 0 & 0 & 0 & 0 & Q_{66} \end{bmatrix} \begin{bmatrix} \xi_{rr} \\ \xi_{\varphi\varphi} \\ \xi_{zz} \\ l_{\varphiz} \\ l_{r\varphi} \end{bmatrix} - \begin{bmatrix} \beta_{11} \\ \beta_{22} \\ \beta_{33} \\ 0 \\ 0 \\ 0 \end{bmatrix} T$$

$$(2)$$

The structural equation of motion is expressed as follows:

$$\frac{\partial \sigma_{rr}}{\partial r} + \frac{\partial \sigma_{r\varphi}}{\partial \varphi} + \frac{\partial \sigma_{rz}}{\partial z} + \frac{1}{r} \left( \sigma_{rr} - \sigma_{\varphi\varphi} \right) = \rho_c \frac{\partial^2 U_r}{\partial t^2}$$
 (3)

$$\frac{\partial \sigma_{r\varphi}}{\partial r} + \frac{\partial \sigma_{\varphi\varphi}}{\partial \varphi} + \frac{2}{r}\sigma_{r\varphi} + \frac{\partial \sigma_{z\varphi}}{\partial z} = \rho_c \frac{\partial^2 U_{\varphi}}{\partial t^2}$$
 (4)

$$\frac{\partial \sigma_{rz}}{\partial r} + \frac{\partial \sigma_{z\varphi}}{r\partial \varphi} + \frac{\sigma_{rz}}{r} + \frac{\partial \sigma_{zz}}{\partial z} = \rho_c \frac{\partial^2 U_z}{\partial t^2}$$
 (5)

Following the state-space method approach, the sixth-order state equations for an orthotropic medium in cylindrical coordinates can be easily derived from the combination of equations (2), (3), and (5).

$$\frac{\partial Y}{\partial r} = MY, Y = \left[ U_r \ U_\varphi \ U_z \ \sigma_{rr} \ \tau_{r\varphi} \ \tau_{rz}, T \right]^t \tag{6}$$

The components along the axes are as follows:

$$\frac{\partial U_z}{\partial r} = \varepsilon_{rz} - \frac{\partial U_r}{\partial z} \tag{7}$$

Using equations (3) through (5) leads to the following equations:

$$\frac{\partial U_z}{\partial z} = \left[ 0 \ 0 \ -\frac{\partial}{\partial z} \ 0 \ 0 \ \frac{1}{Q_{55}} \ 0 \right] (Y) \tag{8}$$

$$\frac{\partial U_{\varphi}}{\partial r} = \varepsilon_{r\varphi} + \frac{U_{\varphi}}{r} - \frac{1}{r} \frac{\partial U_{r}}{\partial \varphi} \tag{9}$$

$$\frac{\partial U_r}{\partial \omega} = \left[ 0 \ \frac{1}{r} - \frac{1}{r} \frac{\partial}{\partial \omega} \ 0 \ \frac{1}{Q_{ee}} \ 0 \ 0 \right] (Y) \tag{10}$$

$$\Rightarrow \frac{\partial U_r}{\partial r} = \varepsilon_{rr} = \begin{bmatrix} -\frac{Q_{13}}{Q_{11}} \frac{\partial}{\partial z} & -\frac{Q_{12}}{Q_{11}} \frac{1}{r} \frac{\partial}{\partial \varphi} & -\frac{Q_{12}}{Q_{11}} \frac{1}{r} & \frac{1}{Q_{11}} & 0 & 0 & \frac{\beta_1}{Q_{11}} \end{bmatrix} (11)$$

$$\Rightarrow \frac{\partial \sigma_{rr}}{\partial r} = \rho_c \frac{\partial^2 U_r}{\partial t^2} - \frac{\partial \sigma_{r\varphi}}{\partial t^2} - \frac{\partial \sigma_{rz}}{r\partial \varphi} - \frac{1}{r} \left( \sigma_{rr} - \sigma_{\varphi\varphi} \right)$$
(12)

Using the dynamic equation, we obtain the following equation:

(15)

$$\frac{\partial \sigma_{rr}}{\partial r} = \left[ \frac{1}{r} \left( Q_{23} - \frac{Q_{12}Q_{13}}{Q_{11}} \right) \frac{\partial}{\partial z}; \frac{1}{r^2} \left( Q_{22} - \frac{Q_{12}^2}{Q_{11}} \right) \frac{\partial}{\partial \varphi}; \left( \rho_c \frac{\partial^2}{\partial t^2} + \frac{1}{r^2} \left( Q_{22} - \frac{Q_{12}^2}{Q_{11}} \right) \right); \frac{1}{r} \left( \frac{Q_{12}}{Q_{11}} - 1 \right) \right]; \left[ -\frac{1}{r} \frac{\partial}{\partial \varphi}; -\frac{\partial}{\partial z}; \left( \frac{\beta_1}{Q_{11}} - \beta_2 \right) \right] (Y)$$

$$(13)$$

Setting: 
$$\zeta_1 = Q_{22} - \frac{Q_{12}^2}{Q_{11}}$$

$$\zeta_2 = Q_{23} - \frac{Q_{12}Q_{13}}{Q_{11}} \tag{14}$$

https://doi.org/10.38124/ijisrt/25nov252

$$\Rightarrow \frac{\partial \sigma_{rr}}{\partial r} = \left[\frac{\zeta_2}{r}\frac{\partial}{\partial z}; \frac{1}{r^2}\zeta_1\frac{\partial}{\partial \varphi}; \left(\rho_c\frac{\partial^2}{\partial t^2} + \frac{\zeta_1}{r^2}\right); \frac{1}{r}\left(\frac{Q_{12}}{Q_{11}} - 1\right); -\frac{1}{r}\frac{\partial}{\partial \varphi}; -\frac{\partial}{\partial z}; \left(\frac{\beta_1}{Q_{11}} - \beta_2\right)\right](Y)$$

$$(16)$$

$$\frac{\partial \sigma_{r\phi}}{\partial r} = \rho_c \frac{\partial^2 U_{\phi}}{\partial t^2} - \frac{\partial \sigma_{\phi\phi}}{r \partial \phi} - \frac{2}{r} \sigma_{r\phi} - \frac{\partial \sigma_{z\phi}}{\partial z} \tag{17}$$

$$\frac{\partial \sigma_{r\varphi}}{\partial r} = \left[ -\left(\frac{\zeta_2 + Q_{44}}{r}\right) \frac{\partial^2}{\partial \varphi \partial z}; \quad \left(\rho_c \frac{\partial^2}{\partial t^2} - \frac{\zeta_1}{r^2} \frac{\partial^2}{\partial \varphi^2} - Q_{44} \frac{\partial^2}{\partial z^2}\right) \right]; \quad \left[\frac{\zeta_1}{r^2} \frac{\partial}{\partial \varphi}; \quad \frac{1}{r} \frac{Q_{12}}{Q_{11}} \frac{\partial}{\partial \varphi}; \quad -\frac{2}{r}; \quad 0; \quad \left(\frac{\beta_1}{Q_{11}} - \beta_2\right) \right] (Y)$$

$$(18)$$

$$\frac{\partial \sigma_{rz}}{\partial r} = -\frac{\partial \sigma_{z\phi}}{r \partial \phi} - \frac{\sigma_{rz}}{r} + \frac{\partial \sigma_{zz}}{\partial z} + \rho_c \frac{\partial^2 U_z}{\partial t^2}$$
(19)

$$\sigma_{z\varphi} = Q_{44} \varepsilon_{z\varphi} = Q_{44} \left( \frac{\partial U_{\varphi}}{\partial z} + \frac{1}{r} \frac{\partial U_{z}}{\partial \varphi} \right) \tag{20}$$

$$\frac{\partial \sigma_{rz}}{\partial r} = \left[ \rho_c \frac{\partial^2}{\partial t^2} - \frac{Q_{44}}{r^2} \frac{\partial^2}{\partial \varphi^2} - \zeta_3 \frac{\partial^2}{\partial z^2}; - \frac{Q_{44}}{r} \frac{\partial^2}{\partial \varphi \partial z} + \frac{\zeta_2}{r} \frac{\partial^2}{\partial \varphi \partial z}; - \frac{\zeta_2}{r\partial z}; - \left( \frac{Q_{13}}{Q_{11}} \frac{\partial \sigma_{rr}}{\partial z} \right); 0; -\frac{1}{r}; \left( \frac{\beta_1}{Q_{11}} - \beta_3 \right) \right] (Y)$$

$$(21)$$

$$\frac{\partial T}{\partial r} = \begin{bmatrix} 0 & 0 & 0 & 0 & 0 & 0 \end{bmatrix} (Y) \tag{22}$$

$$\begin{bmatrix} \frac{\partial U_z}{\partial r} \\ \frac{\partial U_\varphi}{\partial r} \\ \frac{\partial U_\varphi}{\partial r} \\ \frac{\partial U_r}{\partial r} \\ \frac{\partial G_{rr}}{\partial r} \\ \frac$$

$$\frac{\partial Y}{\partial r} = MY \tag{24}$$

Next, by using the appropriate normal mode expansions, the state variable vector Y can be expanded in terms of unknown modal coefficients. The form of the solutions to this state equation is given by [26]:

$$\begin{pmatrix}
U_{z} \\
U_{\varphi} \\
U_{r} \\
\sigma_{rr} \\
\tau_{r\varphi} \\
\tau_{rz} \\
T
\end{pmatrix} = \sum \begin{pmatrix}
jR_{0}\overline{U}_{z,\eta}(\eta) \\
jR_{0}\overline{U}_{\varphi,\eta}(\eta) \\
R_{0}\overline{U}_{r,\eta}(\eta) \\
Q_{44}^{1}\overline{\sigma}_{rr,\eta}(\eta) \\
Q_{44}^{1}\overline{\tau}_{r\varphi,\eta}(\eta) \\
Q_{44}^{1}\overline{\tau}_{r\varphi,\eta}(\eta) \\
T_{0}(\eta)
\end{pmatrix} exp[j(\omega t - K_{iz}z - \eta\varphi)] \tag{25}$$

By solving the structural state equation, we get:

$$U_{z} = \sum j R_{0} \overline{U}_{z,\eta}(\eta) \exp[j(\omega t - K_{iz}z - \eta \varphi)]$$
(26)

Volume 10, Issue 11, November – 2025

ISSN No: -2456-2165

https://doi.org/10.38124/ijisrt/25nov252

$$\frac{\partial U_Z}{\partial r} = \frac{\partial U_T}{\partial r} + \frac{1}{Q_{55}} \sigma_{r_Z} \tag{27}$$

Replacing  $U_r$  and  $\sigma_{rz}$  , we have:

$$\frac{\partial U_z}{\partial r} = \sum \left[ -R_0 \overline{U}_{r,\eta}(\eta) K_{iz} exp[j(\omega t - K_{iz} z - \eta \varphi)] + j \frac{Q_{44}}{Q_{55}} \overline{\sigma}_{rz,\eta}(\eta) exp[j(\omega t - K_{iz} z - \eta \varphi)] \right]$$
(28)

Also:

$$U_{z} = \sum j R_{0} \overline{U}_{z,\eta}(\eta) \exp[j(\omega t - K_{iz}z - \eta\varphi)]$$
(29)

Yet we know that:  $\eta = \frac{r}{R_0} \Longrightarrow dr = R_0 d\eta$ 

$$\frac{\partial U_z}{\partial r} = \sum j R_0 \frac{dU_{z,\eta}(\eta)}{R_0 d\eta} exp[j(\omega t - K_{iz}z - \eta \varphi)]$$
(30)

Equating (28) = (30)

$$\Rightarrow \frac{d\bar{U}_{z,\eta}(\eta)}{d\eta} = \begin{bmatrix} 0 & 0 & R_0 K_{iz} & 0 & 0 & \frac{Q_{44}^1}{Q_{\pi\pi}} & 0 \end{bmatrix} (\bar{Y})$$
(31)

$$\frac{\partial U_{\varphi}}{\partial r} = \frac{1}{r} U_{\varphi} - \frac{1}{r} \frac{\partial U_{r}}{\partial \varphi} + \frac{1}{Q_{ee}} \sigma_{r\varphi} \tag{32}$$

$$\frac{\partial U_{\varphi}}{\partial r} = j \frac{R_0}{r} \overline{U}_{\varphi,\eta}(\eta) + j \frac{\eta R_0}{r} \overline{U}_{r,\eta}(\eta) + j \frac{Q_{44}^1}{Q_{cc}} \overline{\sigma}_{r\varphi,\eta}(\eta)$$
(33)

also:

$$\frac{\partial U_{\varphi}}{\partial r} = \frac{\partial}{\partial \varphi} \left[ \sum j R_0 \overline{U}_{\varphi,\eta}(\eta) exp[j(\omega t - K_{iz}z - \eta \varphi)] \right]$$
(34)

$$\Rightarrow \frac{\partial U_{\varphi}}{\partial r} = \frac{dU_{\varphi}}{d\bar{n}} \tag{35}$$

$$\Rightarrow \frac{d\overline{U}_{\varphi,\eta}(\eta)}{d\overline{\eta}} = \begin{bmatrix} 0 & \frac{1}{\eta} & \frac{n}{\eta} & 0 & \frac{Q_{44}}{Q_{66}} & 0 & 0 \end{bmatrix} (\overline{Y})$$
(36)

$$\frac{\partial U_r}{\partial r} = -\frac{Q_{13}}{Q_{11}} \frac{\partial U_z}{\partial z} - \frac{Q_{12}}{Q_{11}} \frac{1}{r} \frac{\partial U_{\varphi}}{\partial \varphi} - \frac{Q_{12}}{Q_{11}} \frac{1}{r} U_r + \frac{1}{Q_{11}} \sigma_{rr} + \frac{\beta_1}{Q_{11}} T \tag{37}$$

$$\frac{\partial U_r}{\partial r} = -\frac{Q_{13}R_0K_{iz}}{Q_{11}}\bar{U}_{z,\eta} + \frac{Q_{12}}{Q_{11}}\frac{1}{r}nR_0\bar{U}_{\varphi,\eta} - \frac{Q_{12}}{Q_{11}}\frac{R_0}{r}\bar{U}_{r,\eta} + \frac{Q_{44}^1}{Q_{55}}\bar{\sigma}_{rr,\eta} + \frac{\beta_1T_0}{Q_{11}}\bar{T}(\eta)$$
(38)

We obtain:

$$\frac{\partial U_r}{\partial r} = \sum R_0 \frac{d\bar{U}_{r,\eta}}{R_0 d\bar{\eta}} \, \bar{U}_{r,\eta}(\eta) exp[j(\omega t - K_{iz}z - \eta\varphi)] \tag{39}$$

$$\Rightarrow \frac{\partial U_r}{\partial r} = \frac{d\bar{U}_{r,\eta}}{d\bar{\eta}} \tag{40}$$

Equations (40) and (38) give:

$$\Leftrightarrow \frac{d\bar{U}_{r,\eta}}{d\bar{\eta}} = \left[ \frac{Q_{13}}{Q_{11}} R_0 K_{iz} - \frac{Q_{12}}{Q_{11}} \frac{n}{\eta} - \frac{Q_{12}}{Q_{11}} \frac{1}{\eta} - \frac{Q_{44}^1}{Q_{55}} \quad 0 \quad 0 \quad \frac{\beta_1 T_0}{Q_{11}} \right] (\bar{Y})$$

$$(41)$$

$$\frac{\zeta_2}{r}\frac{\partial U_r}{\partial r} + \frac{\zeta_1}{r^2}\frac{\partial U_{\varphi}}{\partial \varphi} + \left(\rho\frac{\partial^2}{\partial t^2} + \frac{\zeta_1}{r^2}\right)U_r + \frac{1}{r}\left(\frac{Q_{12}}{Q_{11}} - 1\right)\sigma_{rr} - \frac{1}{r}\frac{\partial \sigma_{r\varphi}}{\partial \varphi} - \frac{\partial \sigma_{rz}}{\partial z} + \left(\frac{\beta_1}{Q_{11}} - \beta_2\right)T = \frac{\partial \sigma_{rr}}{\partial r} \tag{42}$$

Similarly, by replacing  $U_r$ ,  $U_\varphi$ ,  $U_z$ ,  $\sigma_{rr}$ ,  $\sigma_{r\varphi}$ ,  $\sigma_{rz}$  and T with its expressions, we get the following relationship:

https://doi.org/10.38124/ijisrt/25nov252

$$\frac{d\bar{\sigma}_{rr,\eta}}{d\bar{\eta}} = \left[ \frac{\zeta_2 \alpha}{Q_{44}^4 \eta} \frac{\zeta_1 \eta}{Q_{44} \eta^2} \frac{1}{Q_{44}^4} \left( \beta + \frac{\zeta_1}{\eta^2} \right) \frac{1}{\eta} \left( \frac{Q_{12}}{Q_{11}} - 1 \right) - \frac{n}{\eta} - \alpha \left( \frac{\beta_1}{Q_{11}} - \beta_2 \right) T_0 \right] \bar{Y}$$

$$\tag{43}$$

$$\alpha = K_{iz}R_0 \tag{44}$$

$$\beta = -\rho_c \omega^2 R_0^2 \tag{45}$$

$$\frac{d\bar{\sigma}_{rz,\eta}}{d\bar{\eta}} = \left[\frac{1}{Q_{44}} \left(\beta + \zeta_3 \alpha^2 + \frac{Q_{44}^1 \eta^2}{\eta^2}\right) \frac{(Q_{44}^1 + \zeta_2 \alpha)}{Q_{44} \eta} \frac{\zeta_2 \alpha}{Q_{44} \eta} \frac{Q_{44}^1 \alpha}{Q_{44}} \quad 0 - \frac{1}{\eta} \left(\frac{\beta_1}{Q_{11}} - \beta_3\right) T_0\right] (\bar{Y}) \tag{46}$$

$$\frac{dT}{dn} = [0 \ 0 \ 0 \ 0 \ 0 \ 0](\bar{Y}) \tag{47}$$

$$\frac{d}{d\eta} \begin{bmatrix} \overline{U}_{z,\eta} \\ \overline{U}_{v,\eta} \\ \overline{G}_{r,\eta} \\ \overline{T} \end{bmatrix} = \begin{bmatrix}
0 & 0 & R_0 K_z & 0 & 0 & \frac{Q_{44}}{Q_{55}} & 0 \\
0 & \frac{1}{\eta} & \frac{n}{\eta} & 0 & \frac{Q_{44}}{Q_{66}} & 0 & 0 \\
-\frac{Q_{13}}{Q_{11}} R_0 K_{iz} & -\frac{Q_{12}}{Q_{11}} \frac{n}{\eta} & -\frac{Q_{12}}{Q_{11}} \frac{1}{\eta} & \frac{Q_{44}}{Q_{11}} & 0 & 0 & \frac{\beta_1 T_0}{Q_{11}} \\
\frac{\xi_2 \alpha}{Q_{44} \eta} & \frac{\xi_1 \eta}{Q_{44} \eta^2} & \frac{1}{Q_4} \left(\beta + \frac{\xi_1}{\eta^2}\right) & -\frac{1}{\eta} \left(\frac{Q_{12}}{Q_{11}}\right) & -\frac{n}{\eta} & -\alpha & \left(\frac{\beta_1}{Q_{11}} - \beta_2\right) T_0 \\
\frac{\left(Q_{14}^1 + \xi_2\right)}{Q_{44} \eta} \alpha \eta & \frac{1}{Q_{44}} \left(\beta + Q_{44}^1 \alpha^2 + \frac{\xi_1 \eta^2}{\eta^2}\right) & \frac{1}{Q_4} \left(\frac{\xi_1 n}{Q_{44} \eta^2}\right) & \frac{Q_{12} n}{Q_{11} \eta} & -\frac{2}{\eta} & 0 & \left(\frac{\beta_1}{Q_{11}} - \beta_2\right) T_0 \\
\frac{\left(\beta + \xi_3 \alpha^2 + \frac{Q_{44}^1 n^2}{\eta^2}\right) \frac{1}{Q_{44}} & \frac{\left(\xi_2 + Q_{44}^1\right) \alpha \eta}{Q_{44} \eta} & \frac{\xi_2 \alpha}{Q_{44} \eta} & \frac{Q_{44}^1 \alpha}{Q_{44}} & 0 & -\frac{1}{\eta} & \left(\frac{\beta_1}{Q_{11}} - \beta_3\right) T_0 \\
0 & 0 & 0 & 0 & 0 & 0 & 0
\end{bmatrix}$$
(48)

Cette équation est de la forme :

$$\frac{dV_n}{d\eta} = D_\eta V_\eta \tag{49}$$

Solving this equation for the entire structure is not straightforward because the components of the matrix depend on the thickness. In the current formulation, the elements of the matrix aren't constant; they're functions of the radial coordinate z. Therefore, a direct solution to the equation is very difficult [27-28].

To address this, we'll use the approximate layer model. We'll divide the structure into P sub-layers of very small thickness. This makes the matrix elements constant within each layer. For our study, all sub-layers are perfectly bonded and aligned so their axes of symmetry coincide.

In the j-th layer of the structure, we denote:

$$D_{\eta} = D_{\eta}(j-1) \tag{50}$$

where:

$$\eta = \eta_{j-1} = R_{j-1} \tag{51}$$

The solution to the state equation is as follows:

$$V_{\eta}(\eta) = V_{\eta}(\eta_{j-1}) exp \left[ \left( \eta - \eta_{j-1} \right) D_{\eta}(\eta_{j-1}) \right]$$
 (52)

With,  $c_i = 1, ..., p$ .

Where:

$$\eta_{j-1} = R_0 + (j-1)\frac{h_p}{p} \le \eta \le \eta_j = R_0 + j\frac{h_p}{p}$$
(53)

$$h_p = \frac{h}{n} \tag{54}$$

and:

$$R_i = R_0 + ih_n \tag{55}$$

$$\eta = \eta_j \Longrightarrow V_{\eta}(\eta_j) = V_{\eta}(\eta_{j-1}) exp[(\eta_j - \eta_{j-1})D_{\eta}(\eta_{j-1})] \quad (56)$$

$$\eta_{j} - \eta_{j-1} = \frac{R_0}{R_n} + j \frac{h_p}{p} - \frac{R_0}{R_n} - j \frac{h_p}{R_n} + \frac{h_p}{R_n} = \frac{h_p}{R_n}$$
 (57)

$$\Leftrightarrow V_{\eta}(\eta_{j}) = V_{\eta}(\eta_{j-1}) exp \left[ \frac{h_{p}}{R_{p}} D_{\eta}(\eta_{j-1}) \right]$$
 (58)

$$j = 1 \Longrightarrow V_{\eta}(\eta_1) = V_{\eta}(\eta_0) exp \left[ \frac{h_p}{R_n} D_{\eta}(\eta_0) \right]$$
 (59)

$$j = p - 1 \Longrightarrow V_{\eta}(\eta_{p-1}) = V_{\eta}(\eta_{p-2}) exp\left[\frac{h_p}{R_p} D_{\eta}(\eta_{p-2})\right]$$
(61)

This is the transfer relationship between the lower and upper interface of the first sub-layer of the layer. *j*.

$$j = p \Longrightarrow V_{\eta}(\eta_p) = V_{\eta}(\eta_{p-1}) exp\left[\frac{h_p}{R_p} D_{\eta}(\eta_{p-1})\right]$$
 (62)

$$j = 2 \Longrightarrow V_{\eta}(\eta_2) = V_{\eta}(\eta_1) exp \left[ \frac{h_p}{R_p} D_{\eta}(\eta_1) \right]$$
 (60)

Using the continuity relationships, we have:

$$V_{\eta}(\eta_p) = V_{\eta}(\eta_{p-1}) = \dots = V_{\eta}(\eta_2) = V_{\eta}(\eta_1)$$
 (63)

$$V_{\eta}\left(\eta_{p}\right) = exp\left[\frac{h_{p}}{R_{p}}D_{n}(\eta)\right] exp\left[\frac{h_{p}}{R_{p}}D_{n}(\eta_{1})\right] exp\left[\frac{h_{p}}{R_{p}}D_{\eta}(\eta_{2})\right] \times \dots \dots \times exp\left[\frac{h_{p}}{R_{p}}D_{n}\left(\eta_{p-1}\right)\right] exp\left[\frac{h_{p}}{R_{p}}D_{n}\left(\eta_{p}\right)\right] V_{\eta}(\eta_{0}) \tag{64}$$

$$\Rightarrow V_n(\eta_n) = T_n V_n(\eta_0) \tag{65}$$

 $T_n = (6 \times 6)$  elements of the transfer matrix.

Hence, we have:

## III. RESULTS AND DISCUSSION

$$T_n = exp\left[\frac{h_p}{R_p}D_n(\eta_0)\right] \times \dots \times exp\left[\frac{h_p}{R_p}D_n(\eta_p)\right]$$
 (66)

The characteristics of the materials in the simulations used in this study are summarized in Table 1.

$$T_n = \prod_{j=1}^p exp \left[ \frac{h_p}{R_p} D_n(\eta_{j-1}) \right]$$
 (67)

Table 1 Characteristics of Stainless Steel 1.4571 and Inconel 718 Materials [1, 8].

Material	Stainless steel. 1.4571	Inconel 718
Density (in Kg/m³)	8000	8440
Young's Modulus (GPa at 200°C)	186	267
Poisson's Ratio	0,3	0,28
Thermal expansion (m m <sup>-1</sup> K <sup>-1</sup> 20°C-200°C)	17,5	13

## > Overall Stress Variation in the Metallic Bellows

In the simulations, the metallic bellows was studied for both mechanical loading and thermal heating phases. While the state-space method provided a solid mathematical model, we used Abaqus to simulate the actual behavior and determine which of thermal or mechanical stresses causes faster material deterioration.

The thermomechanical simulations were performed on stainless steel 1.4571 and Inconel 718. The results showed that the Von Mises equivalent stress reached 8222 MPa for stainless steel 1.4571 and 12170 MPa for Inconel 718. The stress on the Inconel 718 was significantly higher than on the stainless steel. We found that the stresses exerted during this phase are most concentrated in the outer convolution of the bellows' free section, which is a key factor in steam circuit malfunctions.

## ➤ Comportement Du Soufflet Métallique

Based on the figure (1 to 3) and the simulation results, several observations can be made on the behavior of the metallic bellows.

The maximum Von Mises equivalent stress is found in the free section of the bellows. This stress reached 8222 MPa for stainl ess steel 1.4571 and 12170 MPa for Inconel 718. The stress on Inconel 718 was significantly higher than on the stainless steel.

These results indicate that while Inconel 718 can withstand higher stress, stainless steel 1.4571 performs comparably well under the given conditions. Therefore, all material parameters must be carefully considered during the manufacturing process to ensure the bellows' integrity.

https://doi.org/10.38124/ijisrt/25nov252

ISSN No: -2456-2165

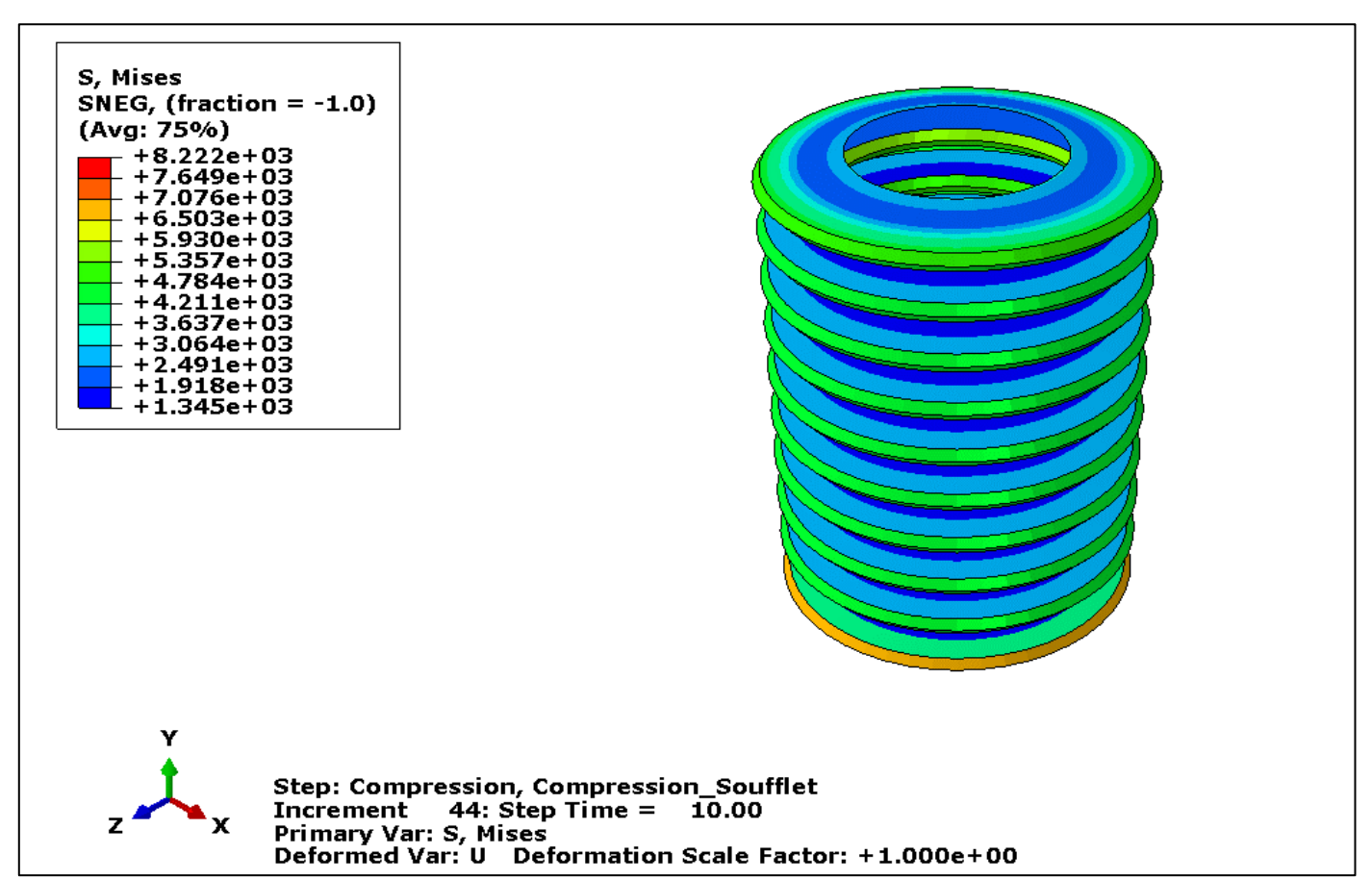


Fig 3 Distribution of the Von Mises Equivalent Stress (in MPa) Under Thermomechanical Loads for Stainless Steel 1.4571.

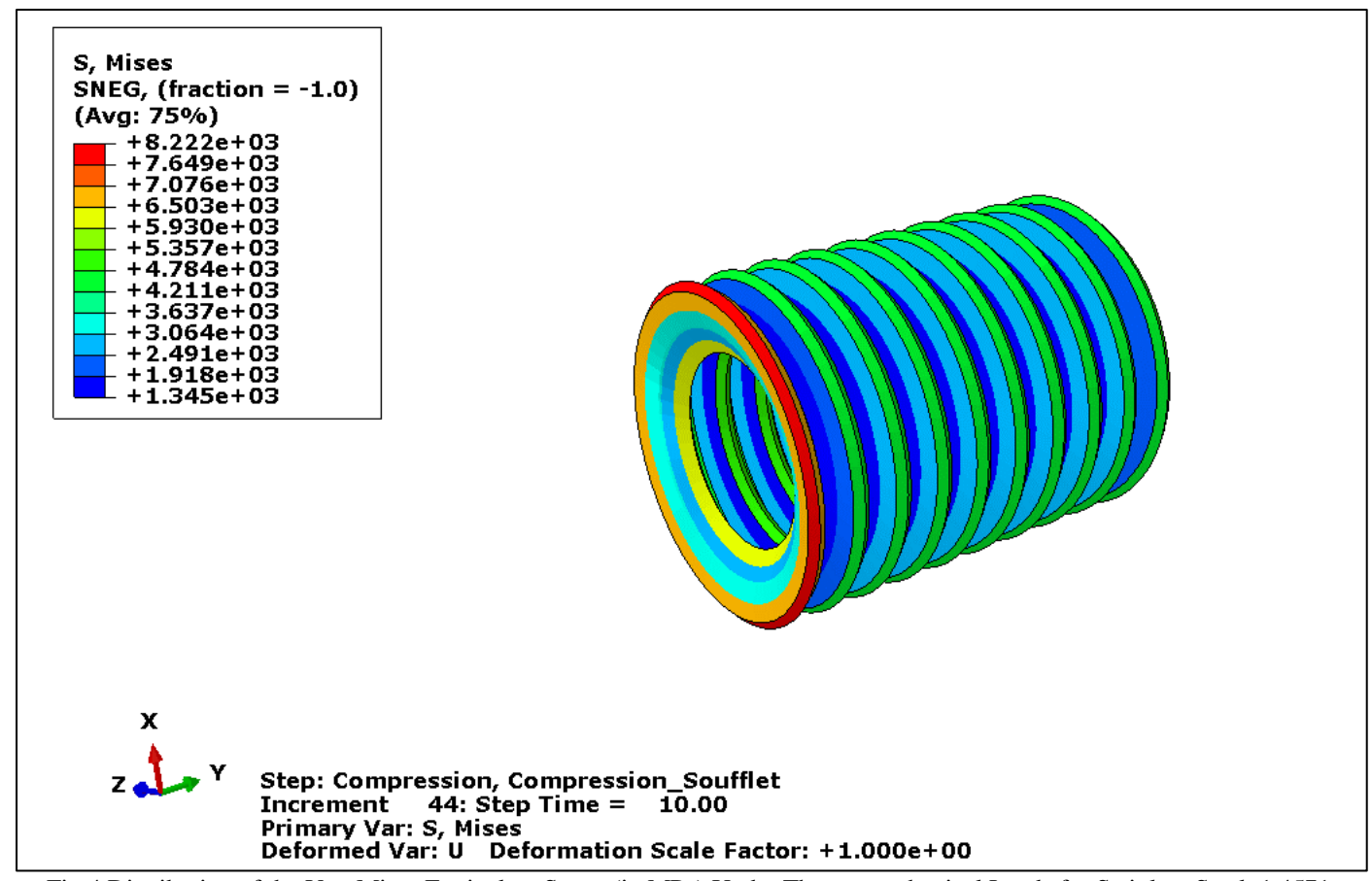


Fig 4 Distribution of the Von Mises Equivalent Stress (in MPa) Under Thermomechanical Loads for Stainless Steel. 1.4571.

https://doi.org/10.38124/ijisrt/25nov252

Volume 10, Issue 11, November – 2025

ISSN No: -2456-2165

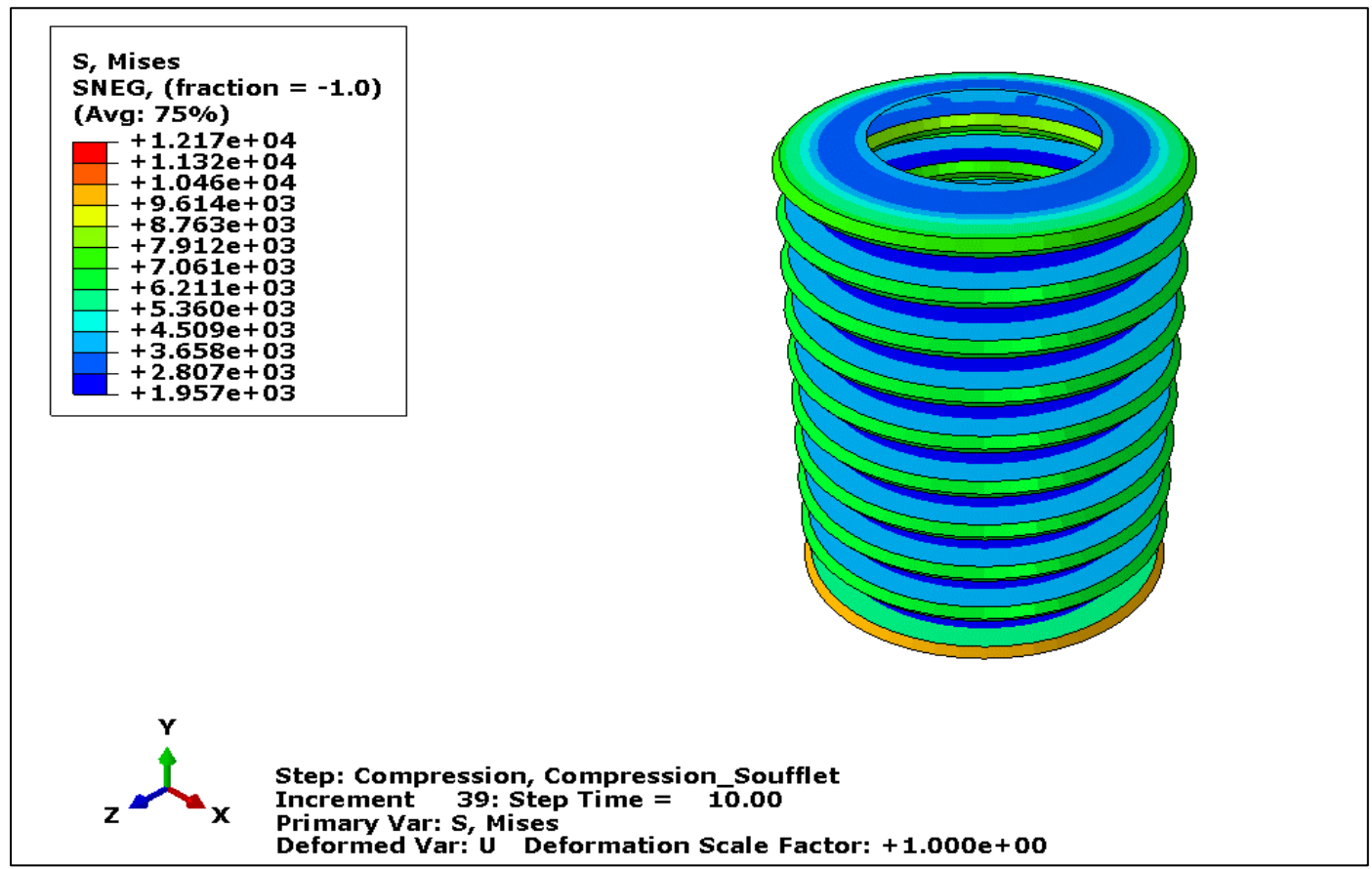


Fig 5 Distribution of the Von Mises Equivalent Stress in MPa Under Thermomechanical Loads for Inconel. 718.

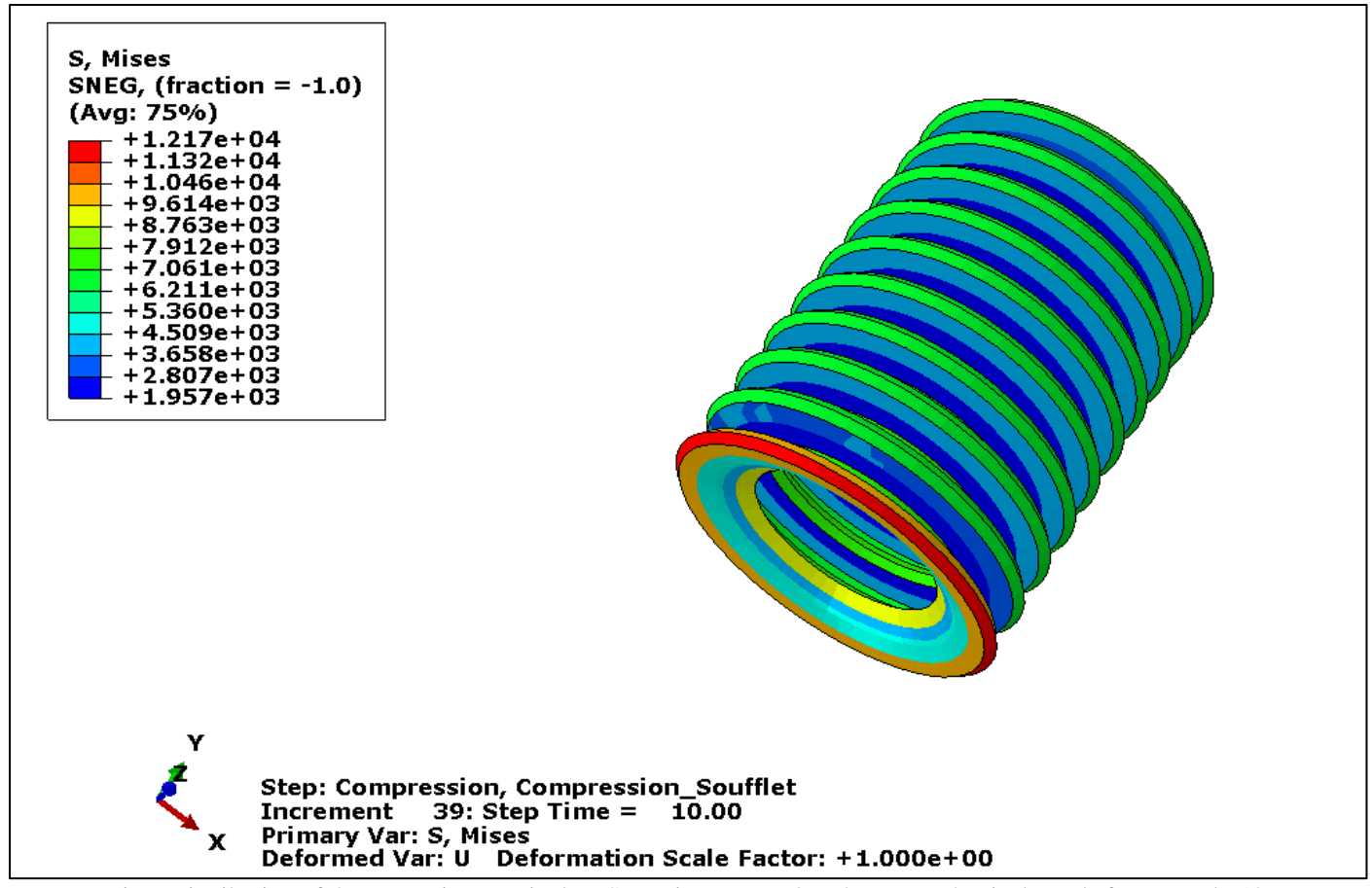


Fig 6 Distribution of the Von Mises Equivalent Stress in MPa Under Thermomechanical Loads for Inconel 718

https://doi.org/10.38124/ijisrt/25nov252

In these simulations, we varied the mass density both above and below a reference value of  $8000~kg/m^3$  to observe its effect on the bellows' behavior. We used values of  $7000~kg/m^3$  and  $9000~kg/m^3$ .

We found that the maximum thermomechanical stress value remained constant regardless of the mass density. This suggests that for the conditions studied, mass density does not have a significant impact on the peak stress experienced by the metallic bellows.

#### ➤ Lifecycles of the Two Materials

The relationships between the maximum stress  $\sigma_{max}$  produced in the bellows and its allowable and fracture lifecycle (N) are expressed as follows [29]:

$$N_A = \left(\frac{563}{\sigma_{max}}\right)^{3,5} \tag{68}$$

$$N_R = \left(\frac{1125}{\sigma_{max}}\right)^{3.5} \tag{69}$$

According to Von Mises, the maximum thermomechanical stresses for Inconel 718 and stainless steel 1.4571 are obtained from simulations, which are then used to determine the materials' lifecycles. The lifecycles of these two materials are summarized in Table 2.

Table 2 Lifecycles of Stainless Steel 1.4571 and Inconel 718 [1, 8]

Material	stainless steel. 1.4571	Inconel 718
$\sigma_{max} (in  kg/mm^2) \times 10^{-2}$	83810,957	124054,895
$N_A$	248	62
$N_R$	2802	710

The acceptable and fracture lifecycles for stainless steel 1.4571 are 248 and 2802 respectively, in contrast to Inconel 718, which has lifecycles of 62 and 710. This demonstrates the superior resistance of the stainless steel to the different stresses.

#### > Thermomechanical Effect

#### Stainless Steel 1.4571

The simulations were conducted at two temperatures, 45°C and 400°C, to study the effects of both mechanical and thermal stresses. The mechanical stresses simulated were the opening and closing of the valve, while the thermal stresses were caused solely by temperature variations.

The results for the 45°C temperature are shown in the following figure 7.

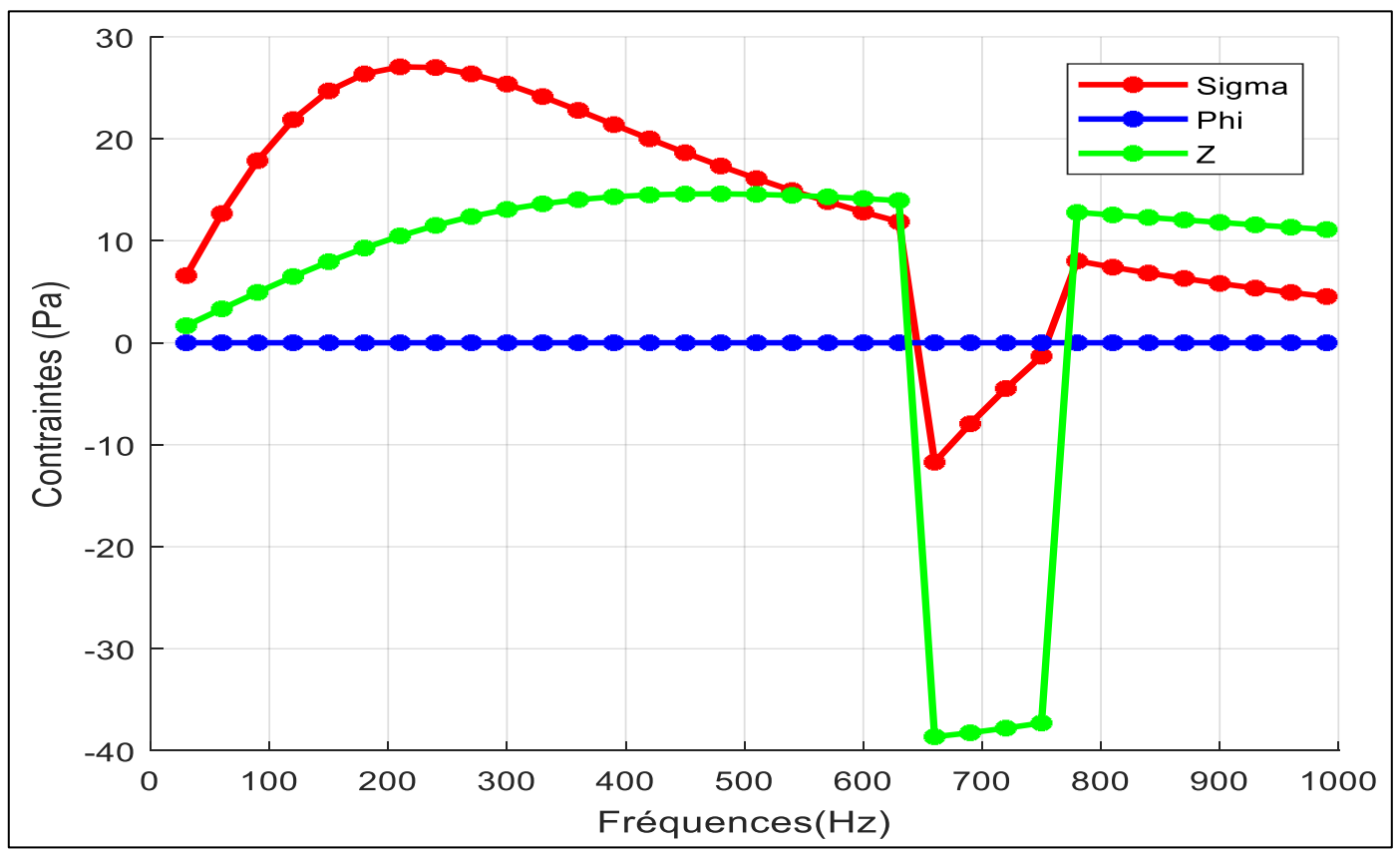


Fig 7 Thermomechanical Stress of Stainless Steel 1.4571 as a Function of Frequency

ISSN No : -2456-2165 https://doi.org/10.38124/ijisrt/25nov252

• This Figure Shows Three Distinct Ranges for the Following Frequency Bands:

#### ✓ First Range:

30 Hz to 630 Hz: In this range, the sigma ( $\sigma$ ) stress is higher than the z stress. The sigma stress reaches a maximum of 27.07 Pa and then decreases with an upward concavity until 630 Hz. The z stress, however, grows from 30 Hz to 390 Hz, reaching an amplitude of 14.32 Pa before stabilizing at this level up to 630 Hz. The phi ( $\phi$ ) stress remains zero throughout this range.

#### ✓ Second Range:

 $630 \, \text{Hz}$  to  $780 \, \text{Hz}$ : Both the sigma ( $\sigma$ ) and z stress curves are negative. They show a trough at  $660 \, \text{Hz}$ , with the sigma stress at -11.71 Pa and the z stress at -38.63 Pa. This range should be avoided as it indicates anti-resonance.

#### ✓ Third Range:

780 Hz to 1000 Hz: This range is notably stable, with both sigma ( $\sigma$ ) and z stresses decreasing. The sigma stress drops from 8.027 Pa to 4.53 Pa, while the z stress decreases from 12.78 Pa to 11.1 Pa.

When temperature is considered for this material, the first two frequency ranges should be avoided due to instability, while the third range shows good stability. This confirms that temperature has a significant influence on the structure.

#### ➤ Results for 400°C

The results for this temperature are shown in the following figure 8.

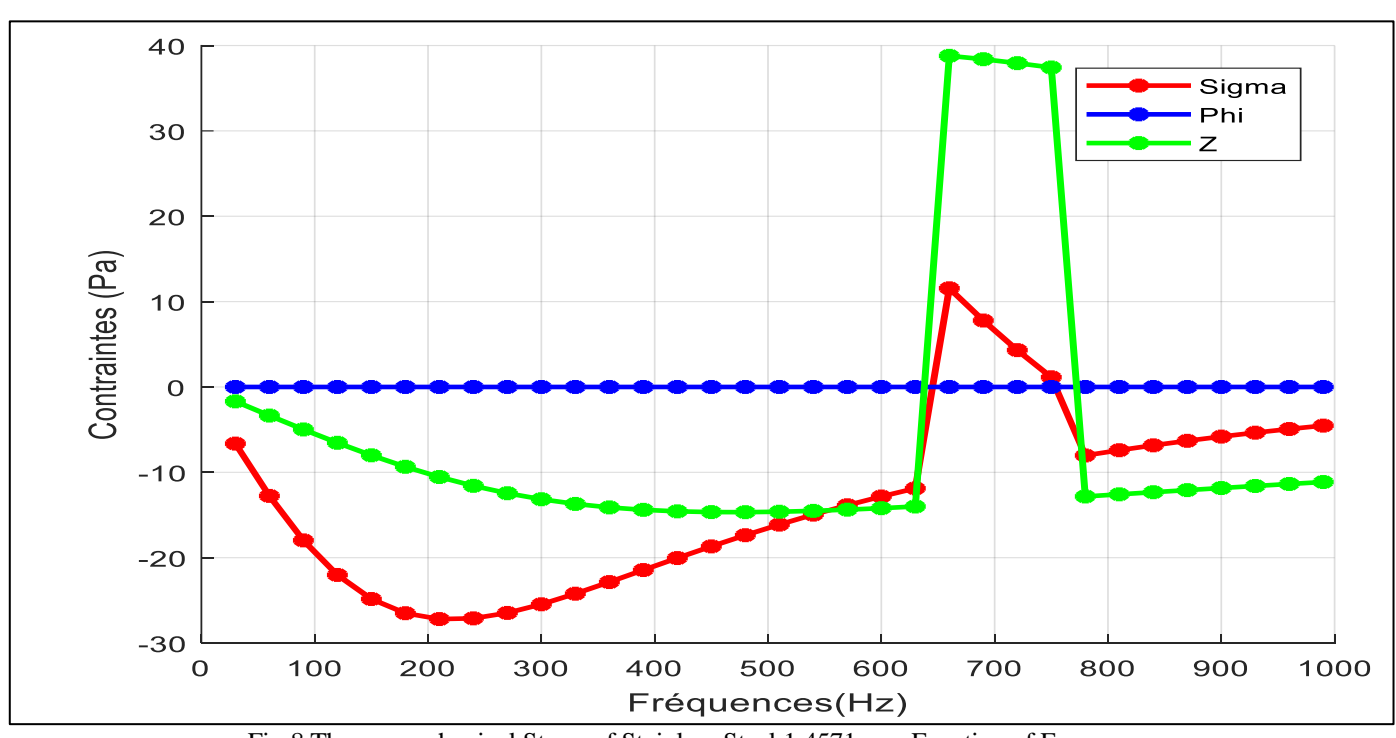


Fig 8 Thermomechanical Stress of Stainless Steel 1.4571 as a Function of Frequency

• At 400°C, We Observe the Inverse Phenomenon Compared to the 45°C Simulation. Three Frequency Ranges Stand Out:

#### ✓ 30 Hz to 630 Hz:

Both sigma ( $\sigma$ ) and z stresses become negative, with the z stress being higher in magnitude than the sigma stress. The z stress decreases from -1.68 Pa to -14.11 Pa and then stabilizes, becoming linear at around -14 Pa. The sigma stress, however, has two parts in this range: it decreases from -6.63 Pa to -27.19 Pa and then increases from -27.11 Pa to -14 Pa.

## ✓ 630 Hz to 780 Hz:

Both the sigma  $(\sigma)$  and z stresses are positive and show a distinct peak. The sigma stress peaks at (660 Hz, 11.56 Pa) and the z stress at (660 Hz, 38.79 Pa). Unlike the  $45^{\circ}\text{C}$  case, this range is considered acceptable.

#### ✓ 780 Hz to 1000 Hz:

In this range, both stress curves for sigma  $(\sigma)$  and z are linear and increase with frequency. The phi  $(\phi)$  stress remains zero.

We can see that at this higher temperature, the sigma  $(\sigma)$  and z stresses are at their maximum in the second frequency range. This suggests that the material can operate optimally for a limited time under these conditions.

## ✓ Inconel 718

Applying the same methodology to Inconel 718. For a temperature of 45°C, the thermomechanical stress curve for Inconel 718 is shown in figure 9.

## ➤ For a Temperature of 45°C

Figure 9 shows the thermomechanical stress curve for Inconel 718 at 45°C.

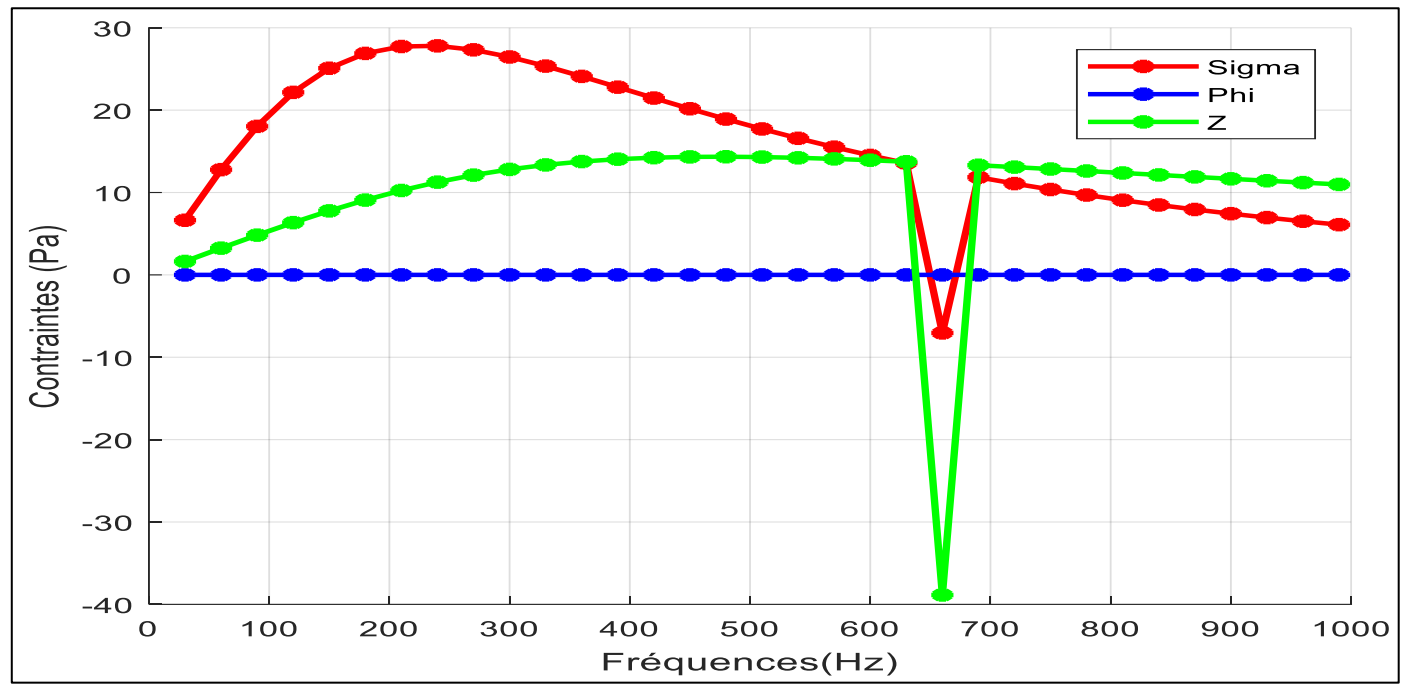


Fig 9 Thermomechanical Stress of Inconel 718 at 45°C

• This Figure Reveals Three Distinct Frequency Ranges for the Material:

## ✓ *First Range (30 Hz to 640 Hz):*

The sigma ( $\sigma$ ) stress shows linear elasticity, while the z stress increases gradually before stabilizing.

## ✓ Second Range (640 Hz to 690 Hz):

Both the sigma  $(\sigma)$  and z stresses drop sharply into the negative range before recovering. The sigma stress plunges to -8 Pa and then rises to 11 Pa. Similarly, the z stress drops to -39 Pa before increasing to 12 Pa. This range should be avoided due to this instability.

## ✓ *Third Range* (690 Hz to 1000 Hz):

Both sigma ( $\sigma$ ) and z stresses are decreasing but show signs of stabilization.

The phi  $(\phi)$  stress remains zero across the entire frequency spectrum.

Overall, the intermediate ranges are recommended for optimal use of the metallic bellows.

# ➤ For a Temperature of 400°C

Figure 10 presents the thermomechanical stresses of Inconel 718 at a temperature of 400°C.

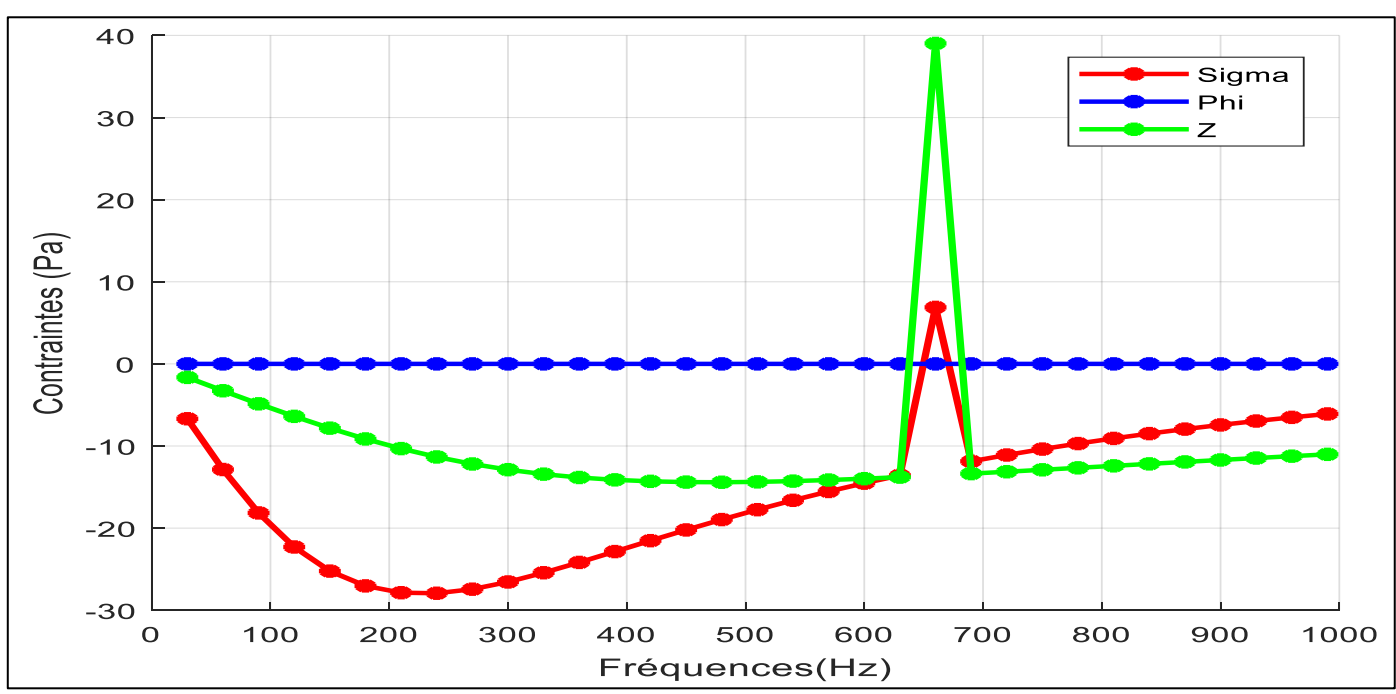


Fig 10 Thermomechanical Stress of Inconel 718 at 400°C

• For Inconel 718 at 400°C, the Inverse Phenomenon Occurs, Similar to the Change Seen with Stainless Steel. Three Distinct Frequency Ranges are Noteworthy:

## ✓ *First Range (30 Hz to 640 Hz):*

The sigma  $(\sigma)$  stress shows a reverse linear elasticity, initially decreasing and then increasing in the negative region. The z stress, however, decreases gradually and then stabilizes.

#### ✓ *Second Range* (640 Hz to 690 Hz):

Both stresses have sharp peaks. The sigma  $(\sigma)$  stress peaks at 8 Pa and then immediately drops to -11 Pa. Similarly, the z stress peaks at 39 Pa and quickly falls to -12 Pa. This area should be avoided.

## ✓ *Third Range (690 Hz to 1000 Hz):*

Both the sigma ( $\sigma$ ) and z stress curves are increasing in the negative region but show signs of stabilization.

The phi (\$\phi\$) stress remains zero across the entire frequency range.

It's important to note that the intermediate ranges are recommended for optimal use of the metallic bellows.

#### IV. DISCUSSION

In this work, we evaluated the life cycles of stainless steel and Inconel 718 metal bellows materials. We have presented the details of allowable and failure life cycles in Table 2. These results demonstrate the performance of 1.4571 stainless steel in comparison to Inconel 718. Our data reflects the steel's resistance to various stresses. The results indicate that all parameters must be considered during the manufacturing process to extend the service life.

We varied the mass density around the reference value. The values of 700 kg/m3 and 9000 kg/m3 were chosen to assess the change in behavior. It appears that in terms of maximum thermomechanical stress, consistency is observed regardless of the mass density value.

With regard to temperature effects, we tested three frequency ranges. We noticed that when temperature is taken into account (45°C and 400°C) for 1.4571 stainless steel, the first two ranges are unstable and should therefore be avoided, unlike the third range, which is stable. Temperature has a significant influence on the structure (Figures 7 and 8). At high temperatures, the sigma ( $\sigma$ ) and z stresses are at their maximum in the second range. The material can function optimally in a short period of time.

For Inconel 718, we conducted the study using the same temperature values and also used three different frequency ranges. The phi  $(\phi)$  stress was zero across the entire frequency range, as shown in Figures 9 and 10. It appears that the intermediate ranges are more suitable for optimal use of the metal bellows.

#### V. CONCLUSION

https://doi.org/10.38124/ijisrt/25nov252

This study presents a thermomechanical stress model for a gate valve with a metallic bellows, focusing on two materials: Inconel 718 and stainless steel 1.4571. Both were subjected to mechanical stresses (opening and closing) and extreme temperature conditions. We used the state-space method to model the thermomechanical stresses during operation. We also calculated the material lifecycles and specific heat capacity. The results from Abaqus/CAE and Matlab allowed us to evaluate the thermomechanical stresses on the bellows, which is crucial for selecting the right material to ensure durability.

Our thermomechanical simulations showed a Von Mises equivalent stress of 8222 MPa for stainless steel 1.4571 and 12170 MPa for Inconel 718. The thermomechanical stress on the stainless steel was lower than that on the Inconel. The acceptable and fracture lifecycles for stainless steel 1.4571 were 248 and 2802, respectively, which are higher than those of Inconel 718 (62 and 710). This confirms that stainless steel has a longer lifespan under these conditions.

Additionally, both at low and high temperatures, we observed specific optimal operating zones and zones of instability.

#### RÉFÉRENCES

- [1]. Popovich AA, Sufiiarov Vsh, Polozov IA and Borisov EV 2015 Microstructure and mechanical properties of inconel 718 produced by slm and subsequent heat treatment *Key Eng. Mat.* 651-653
- [2]. Sieniawski J and Nowotnik A 2010 Effect of thermomechanical working on the micro-structure and mechanical properties of hot pressed superalloy inconel 718 Conference 383-396
- [3]. Malý M., Nopová K, Klakurková L, Adam O, Pantělejev L and Koutný D 2022 Effect of preheating on the residual stress and material properties of inconel 939 processed by laser powder bed fusion *Materials* 15 6360
- [4]. Medeiros S, Prasad Y.V.R.K., Frazier W and Srinivasan R 2000 Microstructural modeling of metadynamic recrystallization in hot working of IN 718 superalloy Mat. Sci. and Eng. A 293 198-207
- [5]. Guimaraes A A and Jonas J J 1981 Recrystallization and aging effects associated with the high temperature deformation of waspaloy and inconel 718 *Metal lurgical Transactions* 293 11
- [6]. Doux A and Vincent P 2019 Thermomechanical modeling of in718 alloy directed energy deposition process *MATEC Web of Conferences* 304 01023
- [7]. Pardo A, Merino M C, Coy A E, Viejo, Carboneras M and Arrabal R 2007 Influence of Ti, C and N concentration on the intergranular corrosion behaviour of AISI 316Ti and 321 stainless steels *Acta Materialia* 55 2239-2251
- [8]. Josip B, Goran T, Čanađija M, and Domagoj L 2011 AISI 316Ti (1.4571) steel-mechanical, creep and

https://doi.org/10.38124/ijisrt/25nov252

- fracture properties versus temperature *J. of Constructl Steel Research* 67 1948-1952
- [9]. Mändl S, Manova D, Neumann H, Pham MT, Richter E and Rauschenbach B 2005 Correlation between piii nitriding parameters and corrosion behaviour of austenitic stainless steels *Surface and Coatings Technology* 200 104-108
- [10]. Jeong K K, Kim Y and Kim K 2010 Influence of Cr, C and NI on intergranular segregation and precipitation in Ti-stabilized stainless steels *Scripta Materialia* 63 449-451
- [11]. Fajnor P, Liptáková T and Konstantova V 2010 Influence of AISI 316Ti stainless stell surface treatment on pitting corrosion in various solutions *Mat. Eng.* 17 12
- [12]. Wang Y, Shao W Z, Zhen L, and Zhang X 2008 Microstructure evolution during dynamic recrystallization of hot deformed superalloy 718 Mater. Sci. and Eng. A 486 321-332
- [13]. Lee K K, Kim H S, Ahn D G, and Lee H 2022 Thermomechanical characteristics of inconel 718 layer deposited on AISI 1045 steel substrate using a directed energy deposition process *J. of Mater. Research and Technology* 17 01
- [14]. Hu YL, Lin X, Li Y, Wang J, Zhang S, Lu X and Huang W 2019 Effect of heat treatment on the microstructural evolution and mechanical properties of gh4099 additive-manufactured by directed energy deposition *J. of Al loys and Compounds* 800
- [15]. Jinoop A N, Christ P, Mishra S and Kushvinder B 2019 Laser additive manufacturing using directed energy deposition of inconel-718 wall structures with tailored characteristics *Vacuum*, 166 270-278 08
- [16]. Zhu G, Shi S H, Fu G F, Shi J, Yang S W, Weidong M and Jiang F 2017 The influence of the substrate-inclined angle on the section size of laser cladding layers based on robot with the inside-beam powder feeding *The Intern. J. of Advanced Manufacturing Techno.* 88 2163-2168
- [17]. Mroziński S, Zbigniew L, and Egner H 2022 Influence of creep damage on the fatigue life of p91 steel *Materials* 15 4917 07
- [18]. Masakazu S, Odum K, and Li G 2019 Investigation of novel trochoidal toolpath strategies for productive and efficient directed energy deposition processes CIRP Anals 68 241244
- [19]. Kim H, Lee KK, Ahn DG and Lee H 2021 Effects of deposition strategy and preheating temperature on thermo-mechanical characteristics of inconel 718 super-alloy deposited on AISI 1045 substrate using a DED process *Materials* 14 1794 04
- [20]. Maleki E, Okan U, Sahebari S, Kashyzadeh KR, and Danilov I 2022 Application of deep neural network to predict the high-cycle fatigue life of AISI 1045 steel coated by industrial coatings *J. of Marine Sci. and Eng.* 10 128 01
- [21]. Wankhede SD and Gawande SH 2023 Design and analysis aspect of metal expansion bellows: A review *Forces in Mechanics* 13 100244
- [22]. Zaki S, Azrar L, and Mouchtachi A 2014 Modeling and numerical simulation of static and dynamic

- behavior of multilayered plates with interface effects *MATEC Web of Conf.* 11 04
- [23]. Nazargah M L and Cheraghi N 2017 An exact peano series solution for bending analysis of imperfect layered fg neutral magneto-electro-elastic plates resting on elastic foundations. *Mech. of Advanced Mater. and Struct.* 24 183-199
- [24]. Lemoine M and Pelgrin F 2003 Introduction aux modèles espace état et au filtre de Kalman *Revue de l'OFCE* (86) 203-229
- [25]. Qatu MS 2004 Vibration of laminated shells and plates. Vibration of Laminated Shells and Plates *American J. of Comput. Mathematics* 1-409
- [26]. Daneshjou K, Shokrieh MM, Moghaddam M G, and Talebitooti R 2010 Analytical model of sound transmission through relatively thick FGM cylindrical shells considering third order shear deformation theory *Comp. Struct.* 93(1) 67-78
- [27]. Rajabi M and Behzad M 2014 Interaction of a plane progressive sound wave with anisotropic cylindrical shells *Comp. Struct.* 116 747-760
- [28]. Zhou Y, Chen W and Lu C 2009 Exact solution for simply supported multiferroic laminates with imperfect interfaces *Symposium of piezoelectricity* 12 92
- [29]. Mohammad A T, Abdulateef J and Hammudi Z 2015 Prediction of Cycle Life of Flexible Pipe Bellows Internat. J. of Mech. Eng. and Applications, 3(1) 6-15.